The Astrophysical Journal Letters, 918:L14 (7pp), 2021 September 1 https://doi.org/10.3847/2041-8213/ac1e2b

# The Discovery of Two LISA Sources within 0.5 kpc

Mukremin Kilic[1], Warren R. Brown[2], A. Bédard[3], and Alekzander Kosakowski[1]
[1] Homer L. Dodge Department of Physics and Astronomy, University of Oklahoma, 440 W. Brooks Street, Norman, OK 73019, USA; kilic@ou.edu, alekzanderkos@ou.edu
[2] Smithsonian Astrophysical Observatory, 60 Garden Street, Cambridge, MA 02138, USA; wbrown@cfa.harvard.edu
[3] Département de Physique, Université de Montréal, C.P. 6128, Succ. Centre-Ville, Montréal, QC H3C 3J7, Canada; bedard@astro.umontreal.ca
*Received 2021 June 10; revised 2021 August 6; accepted 2021 August 16; published 2021 August 27*

## Abstract

We report the discovery of the brightest detached binary white dwarfs with periods less than an hour, which provide two new gravitational-wave verification binaries for the Laser Interferometer Space Antenna (LISA). The first one, SMSS J033816.16−813929.9 (hereafter J0338), is a 30.6 minute orbital period, $g = 17.2$ mag detached double white dwarf binary with a Gaia parallax measurement that places it at a distance of 533 pc. The observed radial velocity and photometric variability provide precise constraints on the system parameters. J0338 contains a $0.230 \pm 0.015\,M_\odot$ white dwarf with a $0.38^{+0.05}_{-0.03}\,M_\odot$ companion at an inclination of $69^\circ \pm 9^\circ$. The second system, SDSS J063449.92+380352.2 (hereafter J0634), is a 26.5 minute orbital period, $g = 17.0$ mag detached double white dwarf binary at a distance of 435 pc. J0634 contains a $0.452^{+0.070}_{-0.062}\,M_\odot$ white dwarf with a $0.209^{+0.034}_{-0.021}\,M_\odot$ companion at an inclination of $37^\circ \pm 7^\circ$. The more massive white dwarf in J0634 is hotter than its companion, even though tidal dissipation is predicted to be relatively inefficient at such periods. This suggests that the more massive white dwarf formed last. J0338 and J0634 will be detected by LISA with a signal-to-noise ratio of 5 and 19, respectively, after four years. We identified these two systems based on their overluminosity and $u$-band photometry. Follow-up of $u$-band selected Gaia targets will likely yield additional LISA verification binaries.

*Unified Astronomy Thesaurus concepts:* Compact binary stars (283); Gravitational wave sources (677); Gravitational waves (678); White dwarf stars (1799)

*Supporting material:* data behind figures

## 1. Introduction

The Laser Interferometer Gravitational-Wave Observatory detected gravitational waves for the first time in late 2015, opening a new window into the universe (Abbott et al. 2016). The source was a binary black hole merger 410 Mpc away. The Laser Interferometer Space Antenna (LISA) mission will expand this window into the mHz frequency range, and will individually resolve tens of thousands of gravitational-wave sources, including (but not limited to) ultracompact binaries, supermassive black hole mergers, and extreme mass ratio inspirals (Amaro-Seoane et al. 2012).

Ultracompact binary white dwarfs are the dominant source class in the mHz gravitational-wave frequency range (Nelemans et al. 2001; Nissanke et al. 2012). Based on binary population synthesis models, LISA will individually resolve ∼25,000 double white dwarfs in the Galaxy (Korol et al. 2017). The number of double white dwarfs that will be detected in both gravitational-wave and electromagnetic observations is much smaller. Korol et al. (2017) estimate 13–24 and 50–73 combined gravitational-wave (with a signal-to-noise ratio of $S/N > 7$) and optical detections from LISA + Gaia and LISA + Vera Rubin Observatory's Legacy Survey of Space and Time (LSST), respectively.

Detection of both electromagnetic and gravitational-wave signals will provide a fantastic opportunity to characterize the double white dwarf population of the Galaxy through precise constraints on the system parameters. For example, knowing the position and the inclination of a binary from electromagnetic data can reduce the uncertainty in the gravitational-wave amplitude by a factor of >40 (Shah et al. 2012, 2013). A precise distance measurement, e.g., from Gaia, can constrain the chirp mass to ∼15%–25% (Shah & Nelemans 2014), while adding orbital decay measurements ($\dot{f}$) reduces it to 0.1%. For the double white dwarf system J1539+5027 (Burdge et al. 2019a), Littenberg & Cornish (2019) estimate that the combination of gravitational-wave and optical measurements will improve its inclination uncertainty by a factor of 5 and its distance uncertainty by a factor of 10.

The Extremely Low-Mass (ELM) Survey discovered the first known examples of detached white dwarf binaries that are strong LISA sources with predicted $S/N = 40$–90 (Brown et al. 2011, 2020a; Kilic et al. 2014). Recently, Burdge et al. (2019a, 2019b, 2020a, 2020b) discovered three additional detached double white dwarf LISA sources with $S/N \approx 90$ based on variable systems identified in the Zwicky Transient Facility (ZTF; Bellm et al. 2019). Their sample includes six additional systems with predicted $S/N \sim 2$–8.

As part of our efforts to identify nearby LISA verification binaries, we have been following up ELM white dwarf candidates identified through Gaia parallaxes and *ugriz* photometry (Kosakowski et al. 2020) from the SkyMapper Southern Survey (SMSS; Onken et al. 2019) and the Sloan Digital Sky Survey (SDSS; Ahumada et al. 2020). Here we present the discovery of two new LISA sources within ≈0.5 kpc. We present our discovery observations and analysis of J0338 and J0634 in Sections 2 and 3, respectively. We discuss the physical parameters of these binaries and their expected gravitational-wave signatures in Section 4, and we conclude.

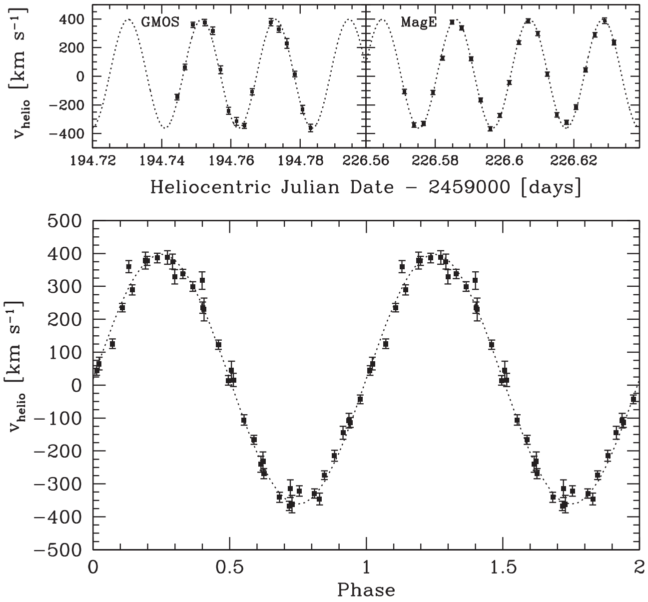

**Figure 1.** Radial velocities of J0338 along with the best-fitting model for a circular orbit (dotted line). The bottom panel shows all of the data points phased with the best-fit period. The radial velocity points are available as the data behind the figure.

(The data used to create this figure are available.)

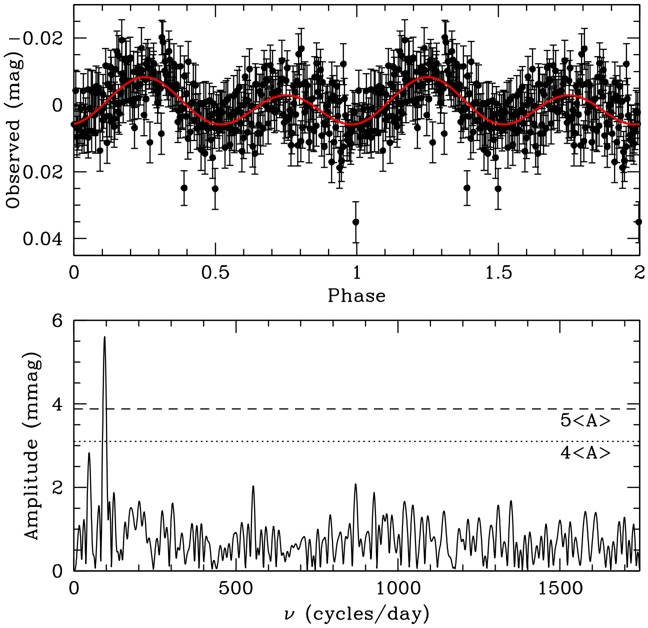

**Figure 2.** Gemini $g$-band light curve of J0338 (top panel) folded at the orbital period, and repeated for clarity. The solid red line displays our best-fitting model. The bottom panel shows the Fourier transform of this light curve, and the $4\langle A\rangle$ and $5\langle A\rangle$ significance levels, where $\langle A\rangle$ is the average amplitude in the Fourier transform.

## 2. SMSS J033816.16−813929.9

### 2.1. Radial Velocity Variability

We obtained optical spectroscopy of J0338 using the 8 m Gemini South telescope equipped with the Gemini Multi-Object Spectrograph (GMOS) as part of the queue program GS-2020B-Q-304 on UT 2020 December 11. We used the B600 grating and a 0.″5 slit, providing wavelength coverage from 3600 to 6735 Å with a resolving power of $R = 1688$. We obtained 17 × 180 s back-to-back exposures over an hour.

Our Gemini data revealed significant radial velocity variability over a 30 minute period. To constrain the orbital period better, we obtained additional spectroscopy on UT 2021 January 12 using the MagE instrument on the 6.5 m Magellan Baade telescope. We used the 0.″85 slit, providing a resolving power of $R = 4800$. We obtained 23 × 215 s back-to-back exposures over 90 minutes.

Figure 1 shows our radial velocity measurements for J0338 along with the best-fitting circular orbit. J0338 shows 759 km s$^{-1}$ peak-to-peak radial velocity variations with a 30.6 minute period. Our model fits to its Balmer line profiles, under the assumption of a single star, indicating $T_{\rm eff} = 18770 \pm 270$ K and $\log g = 6.60 \pm 0.04$, which correspond to $M = 0.230 \pm 0.015\,M_\odot$ and $R = 0.0396 \pm 0.0018\,R_\odot$ based on Althaus et al. (2013) models. Istrate et al. (2016) evolutionary sequences give results consistent with these estimates. Given the mass function, the companion white dwarf has $M \geqslant 0.34 M_\odot$.

### 2.2. Ellipsoidal Variations

We obtained Gemini GMOS time-series photometry of J0338 on UT 2021 January 25 as part of the program GS-2021A-FT-202. We obtained 299 × 7 s back-to-back exposures through an SDSS-$g$ filter. We binned the chip by 4 × 4, which resulted in a plate scale of 0.″32 pixel$^{-1}$ and a 17.7 s overhead, resulting in a cadence of 24.7 s.

Figure 2 shows our Gemini light curve of J0338 and its Fourier transform. The latter shows a significant peak at $94.3 \pm 0.6$ cycles day$^{-1}$, which is half the orbital period measured from the radial velocity data. There is also a smaller peak at the orbital frequency. The top panel shows the light curve folded at the orbital period, and repeated for clarity. J0338 shows evidence of both the Doppler beaming effect (Zucker et al. 2007) and ellipsoidal variations due to a tidally distorted white dwarf.

We perform a simultaneous, nonlinear least-squares fit that includes the amplitude of the Doppler beaming ($\sin\phi$), ellipsoidal variations ($\cos 2\phi$), and reflection ($\cos\phi$). We find the amplitudes of these effects to be $0.25\% \pm 0.05\%$, $0.52\% \pm 0.05\%$, and $0^{+0.03}_{-0.00}\%$, respectively. The amplitude of the Doppler beaming effect is mainly determined by the temperature and radial velocity semiamplitude of the ELM white dwarf (Shporer et al. 2010). The predicted Doppler beaming amplitude for J0338 is exactly the same as the observed amplitude of 0.25%.

The ellipsoidal variation amplitude mainly depends on the mass ratio of the binary, the radius of the primary, and the inclination (Morris & Naftilan 1993). The former can be constrained based on the radial velocity variations, and the radius of the primary can be constrained directly using the spectral energy distribution and fitting for the solid angle $\pi(R/D)^2$, where $R$ is the radius of the star and $D$ is its distance ($D = 533^{+13}_{-14}$ pc for J0338; Bailer-Jones et al. 2021). Hence, the amplitude of the ellipsoidal variations can be used to constrain the inclination of the binary. For J0338, the $0.52\% \pm 0.05\%$ ellipsoidal variation amplitude requires an inclination of $69° \pm 9°$. The lack of eclipses also sets an upper limit on inclination as $\leqslant 78°$. Hence, based on these constraints, the mass of the companion white dwarf is $0.38^{+0.05}_{-0.03}\,M_\odot$.

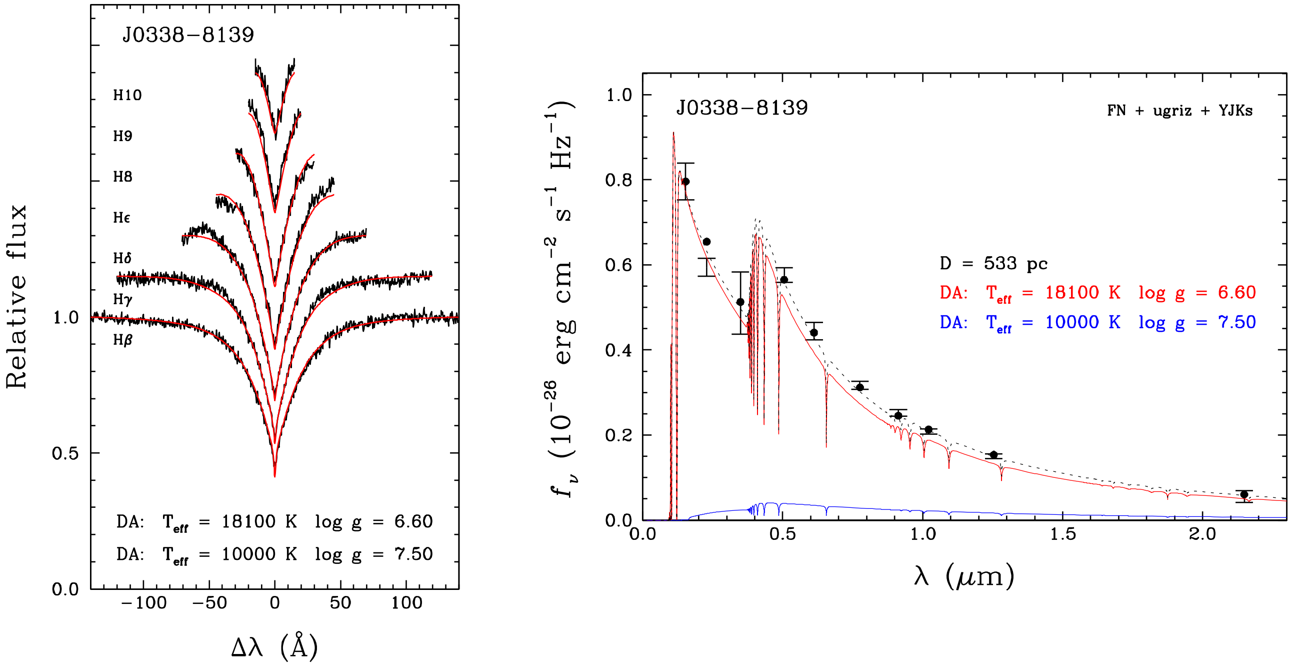

**Figure 3.** Best joint fit to J0338's Balmer lines (left panel) and spectral energy distribution (right panel). The left panel shows the synthetic model (red) overplotted on the observed spectrum (black). The right panel shows the synthetic fluxes (filled circles) and observed fluxes (error bars). The red and blue lines show the contribution of each white dwarf to the total monochromatic model flux, displayed as the black dotted line.

### 2.3. Binary Parameters

Our single-star analysis of the Balmer lines of J0338 yields a spectroscopic distance in good agreement with the Gaia EDR3 parallax, indicating that the primary component largely dominates the observed flux of the system. For this reason, the temperature, radius, and mass of the ELM white dwarf in J0338 are reliably constrained based on optical spectroscopy and Gaia parallax. The mass of the secondary white dwarf and the inclination of the binary are also constrained based on the radial velocity data and the observed ellipsoidal variations.

To constrain the temperature of the secondary white dwarf, we rely on the deconvolution procedure introduced by Bédard et al. (2017), where we fit simultaneously the observed Balmer lines and spectral energy distribution with composite model atmospheres. We use dereddened GALEX FUV and NUV (Martin et al. 2005), SkyMapper *ugriz* (Onken et al. 2019), and VISTA Hemisphere Survey $YJK_s$ photometry (McMahon et al. 2021). Since the observed flux can be expressed as a combination of the individual contributions of the two components, the free parameters usually involved in this fitting process are the four atmospheric parameters $T_{\rm eff,1}$, $\log g_1$, $T_{\rm eff,2}$, $\log g_2$, plus the distance $D$ (see Bédard et al. 2017; Kilic et al. 2020 for details). In the present case, the distance is known from the Gaia parallax, and the surface gravities can be obtained from our mass estimates together with the mass–radius relation of Althaus et al. (2013). Consequently, we fit only for the effective temperatures while holding other parameters fixed. Even though $T_{\rm eff,1}$ is relatively well constrained from our single-star fit to the Balmer lines, it is allowed to vary as it is slightly affected by the addition of a secondary star.

Given our inclination constraints from ellipsoidal variations, there exists a unique fit to the Balmer lines and the spectral energy distribution of this system. Figure 3 shows this best-fitting solution, where the combination of a $18{,}100 \pm 300$ K primary and a $10{,}000 \pm 1000$ K companion provides an excellent match to the data. The secondary star is 14× fainter than the primary star in the $g$ band and hence barely affects the Balmer lines. However, it makes a small contribution to the spectral energy distribution, with the result that the primary white dwarf must be slightly cooler than indicated by the single-star analysis.

## 3. SDSS J063449.92+380352.2

### 3.1. Radial Velocity and Photometric Variability

We obtained a single spectrum of J0634 using the 6.5 m MMT with the Blue Channel spectrograph on UT 2020 December 9. We operated the spectrograph with the 832 line $\rm mm^{-1}$ grating in second order and a $1''$ slit, providing wavelength coverage from 3600 to 4500 Å and a spectral resolution of 1.0 Å. This initial spectrum confirmed J0634 as a low-mass white dwarf.

We obtained time-series optical spectroscopy of J0634 using the 8 m Gemini North telescope equipped with GMOS as part of the queue program GN-2021A-Q-300 on UT 2021 February 12 and March 4. The observing setup was identical to that of J0338 on Gemini South. Our Gemini data revealed significant radial velocity variability over a ≈26 minute period.

To constrain the orbital period better, we obtained additional MMT spectroscopy on March 8–9. Figure 4 shows our radial velocity measurements for J0634 along with the best-fitting circular orbit. J0634 shows 264 $\rm km\,s^{-1}$ peak-to-peak radial velocity variations with a 26.5 minute period.

We acquired high-speed photometry of J0634 over 4.7 hr on UT 2021 February 26 using the APO 3.5 m telescope with the Agile frame transfer camera (Mukadam et al. 2011) and the BG40 filter. We used an exposure time of 10 s and binned the CCD by 2 × 2, which resulted in a plate scale of $0\farcs258$ $\rm pixel^{-1}$.

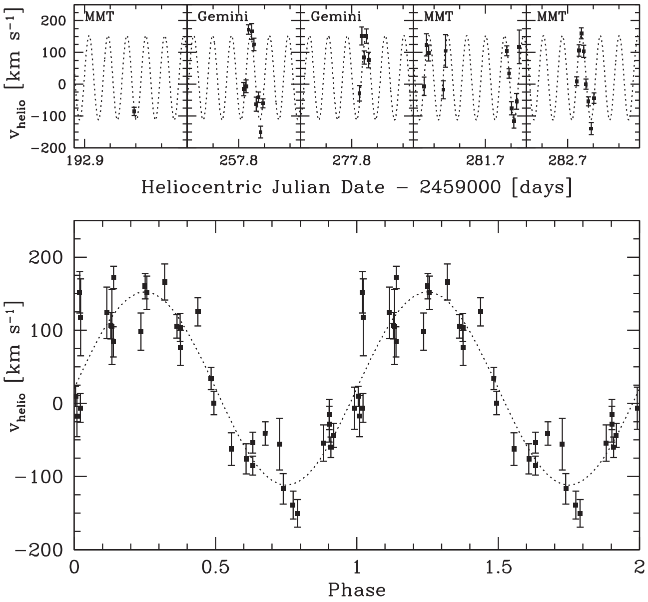

**Figure 4.** Radial velocities of J0634 along with the best-fitting model for a circular orbit (dotted line). The bottom panel shows all of the data points phased with the best-fit period. The radial velocity points are available as the data behind the figure.

(The data used to create this figure are available.)

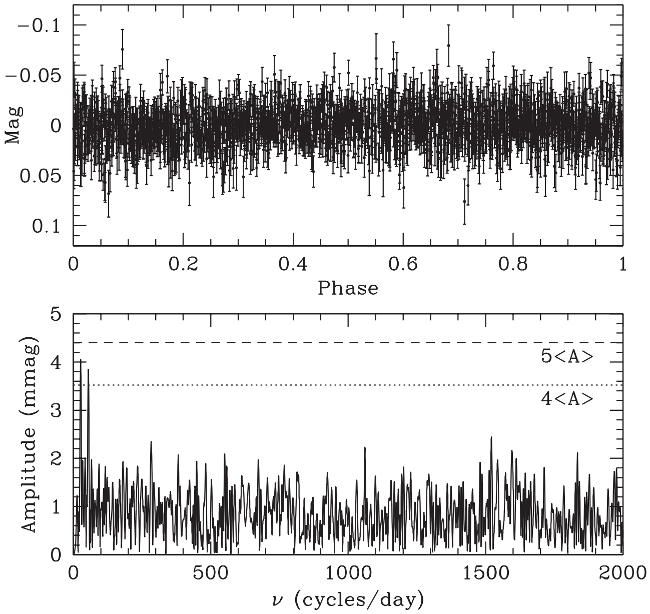

**Figure 5.** APO 3.5 m light curve of J0634 (top panel) folded at the orbital period. The bottom panel shows the Fourier transform of this light curve, and the $4\langle A\rangle$ and $5\langle A\rangle$ significance levels.

Figure 5 shows our APO light curve of J0634 (top panel) and its Fourier transform (bottom panel). The latter shows two peaks at the $4\langle A\rangle$ level, at 0.5× and 1× the orbital frequency. The peak at half the orbital frequency is likely an artifact of the relatively short observing baseline. A Monte Carlo analysis using the `Period04` package (Lenz & Breger 2014) finds an amplitude of $0.34\% \pm 0.12\%$ for the peak at the orbital frequency. Hence, J0634 likely shows low-level sinusoidal variability at the orbital period. Given the lack of ellipsoidal variations, the light curve does not provide any additional constraints on the component masses.

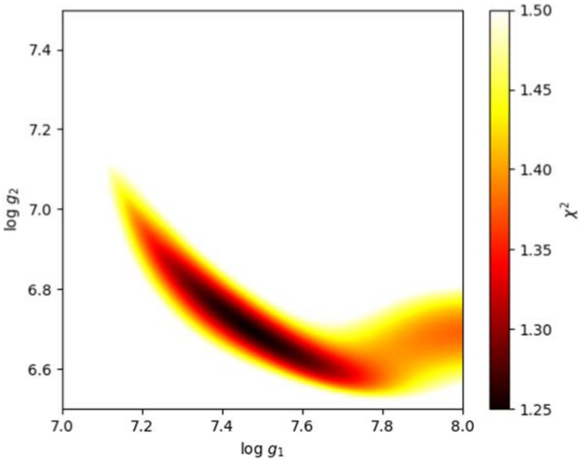

**Figure 6.** $\chi^2$ distribution for our joint analysis as a function of the surface gravity of the primary and secondary stars in J0634. The dark region corresponds to the $\log g_1$ and $\log g_2$ values for which a consistent fit to the spectroscopy and photometry is possible, each solution having its own best-fitting $T_{\rm eff,1}$ and $T_{\rm eff,2}$ values.

### *3.2. Binary Parameters*

The spectroscopic distance estimate for J0634, under the assumption of a single object dominating the light, differs significantly from the Gaia EDR3 parallax, indicating that the companion contributes significant light in this system. Based on the deconvolution procedure from Bédard et al. (2017), fitting the observed Balmer lines and dereddened SDSS *u* and Pan-STARRS *grizy* photometry with $T_{\rm eff,1}$, $\log g_1$, $T_{\rm eff,2}$, and $\log g_2$ all allowed to vary, we find several possible solutions that reproduce the the spectroscopic and photometric data for J0634.

Figure 6 shows the $\chi^2$ distribution of our fits as a function of $\log g_1$ and $\log g_2$. The dark region corresponds to the $\log g_1$ and $\log g_2$ values for which a consistent fit to the spectroscopy and photometry is possible, each solution having its own best-fitting $T_{\rm eff,1}$ and $T_{\rm eff,2}$ values. There are many possible $\log g_1$ and $\log g_2$ solutions along a narrow banana-shaped region. The brighter (primary) star in the system has a higher surface gravity compared to the companion. However, an increase in $\log g_1$ can be compensated by a decrease in $\log g_2$. In other words, a more massive, smaller, and fainter primary requires a less massive, larger, and brighter companion white dwarf to explain the observed spectral energy distribution.

Figure 7 shows the best-fitting solution that lies at the center of the minimum $\chi^2$ region in Figure 6. The observed Balmer lines and *ugrizy* photometry are explained fairly well by a binary system of a primary white dwarf with $(T_{\rm eff}, \log g, M)_1 = (27{,}300\ {\rm K}, 7.46, 0.452\ M_\odot)$ and a secondary white dwarf with $(T_{\rm eff}, \log g, M)_2 = (10{,}500\ {\rm K}, 6.72, 0.209\ M_\odot)$, where the mass estimates are based on the He-core models of Althaus et al. (2013). For comparison, the best-fitting solution at the top left boundary of the dark region in Figure 6 has $(T_{\rm eff}, \log g, M)_1 = (24{,}400\ {\rm K}, 7.24, 0.390\ M_\odot)$, and $(T_{\rm eff}, \log g, M)_2 = (10{,}300\ {\rm K}, 6.91, 0.243\ M_\odot)$, whereas the best-fitting solution at the bottom right boundary has $(T_{\rm eff}, \log g, M)_1 = (31{,}300\ {\rm K}, 7.74, 0.522\ M_\odot)$, and $(T_{\rm eff}, \log g, M)_2 = (10{,}800\ {\rm K}, 6.59, 0.188\ M_\odot)$. In the latter

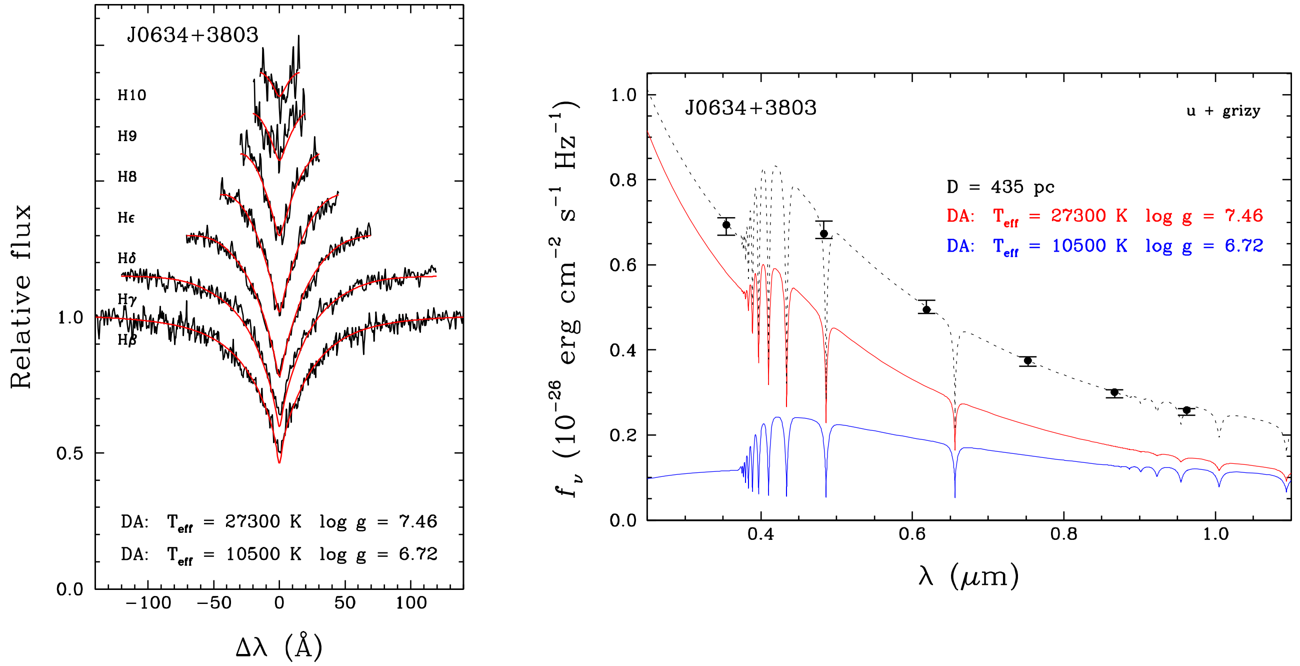

**Figure 7.** Best joint fit to J0634's Balmer lines (left panel) and spectral energy distribution (right panel). The left panel shows the synthetic model (red) overplotted on the observed spectrum (black). The right panel shows the synthetic fluxes (filled circles) and observed fluxes (error bars). The red and blue lines show the contribution of each white dwarf to the total monochromatic model flux, displayed as the black dotted line.

case, the primary lies outside of the parameter space covered by the Althaus et al. (2013) cooling tracks, so we instead used the CO-core models of Bédard et al. (2020) to evaluate $M_1$.

As expected, for all viable solutions, the secondary star contributes appreciably to the total flux. We verified that the best-fitting solution does not predict significant ellipsoidal variations ($\leqslant 0.01\%$) and a detectable double Hα feature at the relatively low resolution of our Gemini spectra. The best-fitting solution would lead to 0.07% and ~0.35% amplitude (Morris & Naftilan 1993) relativistic beaming and reflection effect, respectively. The latter is consistent with the $0.34\% \pm 0.12\%$ observed variability in the APO light curve of J0634. However, additional time-series photometry is needed to confirm the source of variability in this system. We conclude that the primary and secondary white dwarfs in J0634 have masses of $0.452^{+0.070}_{-0.062}\,M_\odot$ and $0.209^{+0.034}_{-0.021}\,M_\odot$, respectively. Based on the mass function, the orbital inclination of this system is $i = 37° \pm 7°$.

## 4. Discussion

J0338 and J0634 are newly identified ultracompact binary systems within ≈0.5 kpc. Table 1 presents the binary parameters for both systems. Both systems involve an ELM white dwarf with a ~0.4 $M_\odot$ white dwarf companion. Figure 8 shows their characteristic strain relative to the 4 yr LISA sensitivity curve (Robson et al. 2019). Open diamonds are previously identified detached binary white dwarfs found in the ELM Survey (Brown et al. 2020b). According to the LISA Detectability Calculator,[4] J0338 and J0634 are estimated to have a 4 yr S/N = 5 and 19, respectively.

Brown et al. (2020a) identified the 20 minute period binary J2322+0509 as the first He + He white dwarf system among the LISA verification binaries. Burdge et al. (2020a, 2020b) identified several additional He + He white dwarf LISA sources. J0338 and J0634 join this list as the brightest and closest members. In fact, J0338 and J0634 are the brightest detached binary white dwarfs currently known with a period less than 1 hr.

Since J0338 shows ellipsoidal variations, follow-up time-series photometry over several years can constrain the rate of period change (e.g., Hermes et al. 2012; Burdge et al. 2019b). With a $\dot{P}$ measurement and the already available constraints on the component masses, orbital inclination, and distance, future

**Table 1**
System Parameters

| Parameter | Value | Value |
|---|---|---|
| Name | J0338 | J0634 |
| R.A. | 03:38:16.16 | 06:34:49.92 |
| Decl. | −81:39:29.9 | +38:03:52.2 |
| $d$ (pc) | $533^{+13}_{-14}$ | $435^{+17}_{-15}$ |
| $u$ (mag) | $17.426 \pm 0.144$ | $17.111 \pm 0.018$ |
| $g$ (mag) | $17.204 \pm 0.009$ | $17.001 \pm 0.010$ |
| $r$ (mag) | $17.438 \pm 0.047$ | $17.285 \pm 0.009$ |
| $E(B-V)$ (mag) | 0.059 | 0.153 |
| $P$ (s) | $1836.1 \pm 31.9$ | $1591.4 \pm 28.9$ |
| $K$ (km s$^{-1}$) | $379.7 \pm 4.6$ | $132.1 \pm 6.0$ |
| $\gamma$ (km s$^{-1}$) | $18.0 \pm 3.8$ | $20.3 \pm 4.3$ |
| $T_{\rm eff,1}$ (K) | $18100 \pm 300$ | $27300^{+4000}_{-2900}$ |
| $\log g_1$ (cm s$^{-2}$) | $6.60 \pm 0.04$ | $7.46^{+0.28}_{-0.22}$ |
| $M_1$ ($M_\odot$) | $0.230 \pm 0.015$ | $0.452^{+0.070}_{-0.062}$ |
| $T_{\rm eff,2}$ (K) | $10000 \pm 1000$ | $10500^{+300}_{-200}$ |
| $\log g_2$ (cm s$^{-2}$) | $7.50^{+0.12}_{-0.09}$ | $6.72^{+0.19}_{-0.13}$ |
| $M_2$ ($M_\odot$) | $0.38^{+0.05}_{-0.03}$ | $0.209^{+0.034}_{-0.021}$ |
| $i$ (°) | $69 \pm 9$ | $37 \pm 7$ |

**Note.** The primary and secondary star parameters in J0634 are highly anticorrelated (see Figure 6 and Section 3.2).

---

[4] https://heasarc.gsfc.nasa.gov/lisa/lisatool/

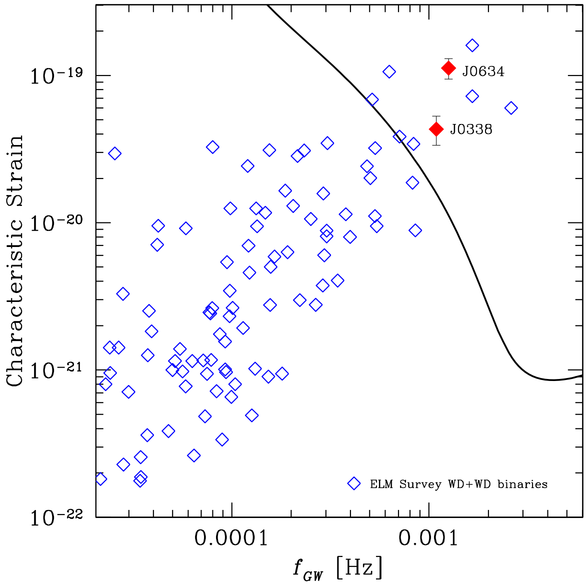

**Figure 8.** Characteristic strain vs. gravitational-wave frequency for J0338, J0634, and other detached white dwarf binaries found in the ELM Survey (open diamonds; Brown et al. 2020b). Solid line is the LISA 4 yr sensitivity curve (Robson et al. 2019).

gravitational-wave measurements will open the door for measuring tidal dissipation in white dwarfs (Fuller & Lai 2013; Piro 2019).

Even though J0338 and J0634 have comparable orbital periods and component masses, the temperatures of the primary and secondary stars are inverted in J0634, where the more massive star is significantly hotter than its companion. Tidal energy dissipation within a white dwarf can increase its surface temperature. Burdge et al. (2019a) estimate that tidal heating alone can heat up the primary white dwarf in the 7 minute orbital period system, ZTF J1539 + 5027, to ≈19,000 K. Though, this is still much lower than the observed temperature of 48,900 K, and intermittent accretion may be responsible for the observed heating of the primary star in that system.

Fuller & Lai (2013, see their Figure 8) show that tidal heating makes a significant contribution to the luminosity for ~10 minute orbital period systems, but it becomes relatively insignificant at ~30 minute periods since $T_{\rm tide} \propto \left(\frac{|\dot{P}|}{P^3}\right)^{1/4}$. Hence, tidal heating cannot explain the inverted temperatures of the primary and secondary stars in J0634.

There are other examples of short-period double white dwarfs with inverted temperatures between the primary and secondary stars (Bours et al. 2015). For example, ZTF J1749 +0924 is similar to J0634 in its characteristics; it has an orbital period of 26.43 minutes and the 0.40 $M_\odot$ primary is significantly hotter than the 0.28 $M_\odot$ secondary (Burdge et al. 2020b).

The temperature difference suggests that the more massive white dwarf formed last. This is expected for some systems evolving through stable and then unstable mass transfer. Studying the formation channels for double white dwarfs, Ruiter et al. (2010) note that the detached systems typically evolve from progenitors with comparable masses, and that the number of detached He–CO white dwarf binaries in which the He white dwarf forms first (i.e., the HeCO-D1 systems in their Table 1) is comparable to the number of binaries in which the CO white dwarf forms first (the COHe-D1 systems). Hence, J0338 and J0634 may simply represent the different outcomes of double white dwarf formation channels.

There are currently 14 detached double white dwarfs known with $P < 40$ minutes, including J0338 and J0634. Five were discovered in the ELM Survey (Brown et al. 2020b) and seven in the ZTF (Burdge et al. 2020a, 2020b). All 14 of these systems contain a white dwarf hotter than 16,000 K. This is not surprising. Given the ~Myr merger timescales for these ultracompact binaries, such systems are rare, and we are more likely to find the brightest and hottest (and therefore youngest) systems in magnitude-limited surveys. J0338 and J0634 have $M_g = 8.2$–$8.4$ mag and dereddened $u - g = 0.13$ and $-0.06$ mag, respectively. Hence, an excellent way to find more of these systems is through follow-up of nearby blue overluminous objects like J0338 and J0634.

The ELM Survey (Brown et al. 2010, 2020b; Kilic et al. 2010) and ZTF (Burdge et al. 2019a, 2020a, 2020b) have explored ELM white dwarf candidates in the northern sky. The *ugriz* photometry from the SkyMapper Southern Survey provides an excellent opportunity to find the brightest ELM white dwarfs in the southern sky, and we are currently following up additional SkyMapper targets as part of the ELM Survey South (Kosakowski et al. 2020). The 10 yr Rubin Observatory Legacy Survey of Space and Time (LSST) and the BlackGEM (Groot et al. 2019) survey will provide both *u*-band photometry and multiepoch photometry in several filters, which will provide a fantastic opportunity to significantly increase the number of double white dwarfs that are LISA sources.

This work was supported in part by the NSF under grant AST-1906379, the Smithsonian Institution, the NSERC Canada, and by the Fund FRQ-NT (Québec).

Based on observations obtained at the Gemini, MMT, and Apache Point Observatory. Gemini is operated by the Association of Universities for Research in Astronomy, Inc., under a cooperative agreement with the NSF on behalf of the Gemini partnership: the National Science Foundation (United States), National Research Council (Canada), CONICYT (Chile), Ministerio de Ciencia, Tecnología e Innovación Productiva (Argentina), Ministério da Ciência, Tecnologia e Inovação (Brazil), and Korea Astronomy and Space Science Institute (Republic of Korea).

The MMT is a joint facility of the Smithsonian Institution and the University of Arizona. The Apache Point Observatory 3.5 m telescope is owned and operated by the Astrophysical Research Consortium.

*Facilities:* Gemini:North and South (GMOS spectrograph), Magellan:Clay (MagE spectrograph), APO 3.5 m (Agile).

## ORCID iDs

Mukremin Kilic https://orcid.org/0000-0001-6098-2235
Warren R. Brown https://orcid.org/0000-0002-4462-2341
A. Bédard https://orcid.org/0000-0002-2384-1326
Alekzander Kosakowski https://orcid.org/0000-0002-9878-1647

## References

Abbott, B. P., Abbott, R., Abbott, T. D., et al. 2016, PhRvL, 116, 061102
Ahumada, R., Allende Prieto, C., Almeida, A., et al. 2020, ApJS, 249, 3
Althaus, L. G., Miller Bertolami, M. M., & Córsico, A. H. 2013, A&A, 557, A19
Amaro-Seoane, P., Aoudia, S., Babak, S., et al. 2012, CQGra, 29, 124016

Bailer-Jones, C. A. L., Rybizki, J., Fouesneau, M., Demleitner, M., & Andrae, R. 2021, AJ, 161, 147

Bédard, A., Bergeron, P., Brassard, P., & Fontaine, G. 2020, ApJ, 901, 93

Bédard, A., Bergeron, P., & Fontaine, G. 2017, ApJ, 848, 11

Bellm, E. C., Kulkarni, S. R., Graham, M. J., et al. 2019, PASP, 131, 018002

Bours, M. C. P., Marsh, T. R., Gänsicke, B. T., et al. 2015, MNRAS, 450, 3966

Brown, W. R., Kilic, M., Allende Prieto, C., & Kenyon, S. J. 2010, ApJ, 723, 1072

Brown, W. R., Kilic, M., Bédard, A., Kosakowski, A., & Bergeron, P. 2020a, ApJL, 892, L35

Brown, W. R., Kilic, M., Hermes, J. J., et al. 2011, ApJL, 737, L23

Brown, W. R., Kilic, M., Kosakowski, A., et al. 2020b, ApJ, 889, 49

Burdge, K. B., Coughlin, M. W., Fuller, J., et al. 2019a, Natur, 571, 528

Burdge, K. B., Coughlin, M. W., Fuller, J., et al. 2020a, ApJL, 905, L7

Burdge, K. B., Fuller, J., Phinney, E. S., et al. 2019b, ApJL, 886, L12

Burdge, K. B., Prince, T. A., Fuller, J., et al. 2020b, ApJ, 905, 32

Fuller, J., & Lai, D. 2013, MNRAS, 430, 274

Groot, P., Bloemen, S., & Jonker, P. 2019, in The La Silla Observatory—From the Inauguration to the Future (Garching : ESO), 33

Hermes, J. J., Kilic, M., Brown, W. R., et al. 2012, ApJL, 757, L21

Istrate, A. G., Marchant, P., Tauris, T. M., et al. 2016, A&A, 595, A35

Kilic, M., Bédard, A., Bergeron, P., & Kosakowski, A. 2020, MNRAS, 493, 2805

Kilic, M., Brown, W. R., Allende Prieto, C., Kenyon, S. J., & Panei, J. A. 2010, ApJ, 716, 122

Kilic, M., Brown, W. R., Gianninas, A., et al. 2014, MNRAS, 444, L1

Korol, V., Rossi, E. M., Groot, P. J., et al. 2017, MNRAS, 470, 1894

Kosakowski, A., Kilic, M., Brown, W. R., & Gianninas, A. 2020, ApJ, 894, 53

Lenz, P., & Breger, M. 2014, Period0: Statistical Analysis of Large Astronomical Time Series, Astrophysics Source Code Library, 4, ascl:1407.009

Littenberg, T. B., & Cornish, N. J. 2019, ApJL, 881, L43

Martin, D. C., Fanson, J., Schiminovich, D., et al. 2005, ApJL, 619, L1

McMahon, R., Banerji, G., Gonzalez, E., et al. 2021, Msngr, 154, 35

Morris, S. L., & Naftilan, S. A. 1993, ApJ, 419, 344

Mukadam, A. S., Owen, R., Mannery, E., et al. 2011, PASP, 123, 1423

Nelemans, G., Yungelson, L. R., & Portegies Zwart, S. F. 2001, A&A, 375, 890

Nissanke, S., Vallisneri, M., Nelemans, G., & Prince, T. A. 2012, ApJ, 758, 131

Onken, C. A., Wolf, C., Bessell, M. S., et al. 2019, PASA, 36, e033

Piro, A. L. 2019, ApJL, 885, L2

Robson, T., Cornish, N. J., & Liu, C. 2019, CQGra, 36, 105011

Ruiter, A. J., Belczynski, K., Benacquista, M., Larson, S. L., & Williams, G. 2010, ApJ, 717, 1006

Shah, S., & Nelemans, G. 2014, ApJ, 791, 76

Shah, S., Nelemans, G., & van der Sluys, M. 2013, A&A, 553, A82

Shah, S., van der Sluys, M., & Nelemans, G. 2012, A&A, 544, A153

Shporer, A., Kaplan, D. L., Steinfadt, J. D. R., et al. 2010, ApJL, 725, L200

Zucker, S., Mazeh, T., & Alexander, T. 2007, ApJ, 670, 1326